Ice-flow-induced scattering zone within the Antarctic ice sheet revealed by high-frequency airborne radar

Kenichi MATSUOKA,[1] Seiho URATSUKA,[2] Shuji FUJITA,[3] Fumihiko NISHIO[4]
[1]Department of Earth and Space Sciences, Box 351310, University of Washington, Seattle, Washington 98195-1310, U.S.A.
E-mail: matsuoka@ess.washington.edu
[2]National Institute of Information and Communications Technology, Nukui-kita 4-2-1, Koganei, Tokyo 184-8795, Japan
[3]National Institute of Polar Research, Kaga, Itabashi ku, Tokyo 173–8515, Japan
[4]Center for Environmental Remote Sensing, Chiba University, 1-33, Yayoi cho, Inage ku, Chiba 263-8522, Japan

ABSTRACT. To better understand how internal radar echoes depend on ice-flow conditions and radar polarization, we surveyed two basins in East Antarctica using 179 MHz airborne radar. We compared radar echoes from three ice-flow conditions: parallel sheet flow in the main stream of a basin, convergent flow towards an ice stream, and longitudinal compression by nunataks. We detected a distinct zone of high radar scattering several hundred meters thick at middle depths in the latter two regions. This high-scattering zone was detected only when the radar polarization plane was parallel to the compression axis in ice. Such a high-scattering zone was not found in the parallel-flow region, regardless of the polarization. Using a recently developed theory of radar scattering in ice, we interpret the high-scattering zone as being caused by crystal-orientation-fabric alternations among adjacent ice layers due to difference in horizontal strain components. We argue that the spatial variation of the high-scattering zone is crucial for understanding past and present flow features.

1. INTRODUCTION

A better understanding of how ice sheets behave over glacial and interglacial cycles requires more knowledge of the processes controlling ice dynamics. The alignment of crystals in ice, called crystal-orientation fabrics (COFs), has an important effect on ice deformation. As ice deforms, non-uniform COFs are produced which, in turn, influence further deformation (e.g. Budd and Jacka, 1989; Azuma, 1994). Consequently, measurements of COF variations can help reveal the deformation history of the ice and indicate how deformation will continue in the future.

Radio waves are well known to scatter from acidity and density non-uniformities in ice sheets (e.g. Clough, 1977; Miller, 1981). Less well known is scattering from non-uniformities in COFs. From laboratory experiments, it is known that the permittivity at radio frequencies is about 1% larger for the component with polarization along the *c* axis as compared to other polarizations (Fujita and others, 1993). This anisotropy can explain why COF variations likely cause radio-wave scattering. For example, a radar survey in eastern Dronning Maud Land, Antarctica, showed that contrasts of COF strength between layers are likely to develop where large amounts of ice shearing are expected and COF non-uniformity is a major source of internal scattering (Fujita and others, 1999). With the use of 60 MHz radar data, similar features of ice layering were found around Vostok lake (Siegert and Kwok, 2000) and Dome C, Antarctica (Siegert and Fujita, 2001). More recently, a spot survey at an ice-coring site in eastern Dronning Maud Land found that anisotropic features in radar echoes at 179 MHz were caused by anisotropic COF patterns (Fujita and others, 2003). Matsuoka and others (2003) found that this feature was continuous over a horizontal distance of 300 km. These studies have established COF variations as a major radar scattering mechanism, at least in East Antarctica, a finding that we rely upon to interpret our measurements in this study.

Although there is a large variety of ice-flow conditions responsible for COF development, no measurements have been made where the ice has parallel flow or longitudinal compression by nunataks. In particular, the latter is dominant along the Antarctic Peninsula, for >1000 km along the Transantarctic Mountains, and for >2000 km along the coast of Dronning Maud Land. In addition, smaller nunataks occupy a major portion of the coasts of Antarctica and Greenland. Furthermore, because the previous measurement in a convergent-flow region was done only in the mid-stream region, we have no knowledge of the COF features in the region further downstream towards the ice streams. Therefore, to broaden the applicability of high-frequency radar as a tool for measuring COFs and to gain better understanding of ice viscosity due to COFs over wide areas, it is important to investigate the spatial variations of COF echoes from ice with different flow conditions.

Here we present results of an airborne radar survey in adjacent basins in eastern Dronning Maud Land with different flow conditions. We found a distinct zone of large radar echoes at depths of 700–1200 m in the convergent-flow region and on the stoss side of nunataks, which cause longitudinal compression. This scattering zone emerged only when the polarization plane was parallel to the horizontal compression axis. In contrast, no such zone was observed in the parallel-flow region. We interpret this polarization-dependent difference to indicate distinct COF patterns that depend on regional-scale ice-flow characteristics.

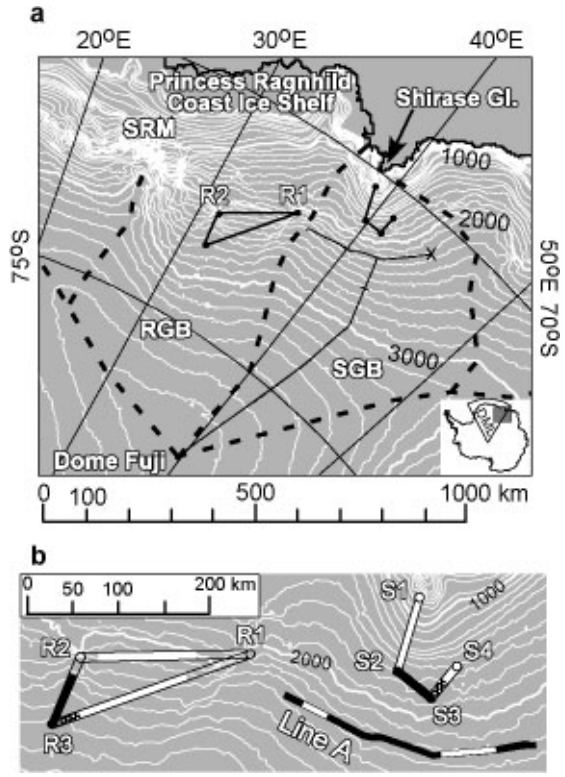

Fig. 1. (a) Ragnhild Glacier basin (RGB) and Shirase Glacier basin (SGB) in eastern Dronning Maud Land, Antarctica (Liu and others, 1999). The shaded rectangle in the inset map shows the area covered by the larger map. RGB has a chain of inland nunataks about 200 km from the coast that include the Yamato Mountains near R1, the Belgica Mountains near R2, and the Sør Rondane Mountains (SRM). This chain of nunataks and wide ice shelves characterize the Dronning Maud Land coast from 20° W to 35° E. Contour intervals are 100 m, and elevations of 1000, 2000 and 3000 m are labeled. Black dashed lines highlight topographic divides. Flight-lines are shown as thick black lines. Thin solid lines in SGB show three previous ground-based measurement lines (Matsuoka and others, 2003) including the Mizuho ice-coring site marked with an X. (b) The flight path and the locations of the continuous high-P_r zone. The locations of the flight turning points are marked with letters and listed in Table 1. We denote the distances counterclockwise along these lines in RGB and SGB as x_R and x_S, respectively. Solid black lines mark the locations of the high-P_r zone, the white-filled lines show locations where this zone was not detected, and the hatched-line segments mark regions with less distinct high-P_r zones. The polarization was parallel to the flight path. We could not distinguish internal scattering and off-nadir bed scattering around R1 and R2. Line A is the lowest line in our previous study (Matsuoka and others, 2003). Spatial variations of the high-P_r zone due to P_{COF}-based anisotropic reflection zones along line A are marked in the same way.

2. STUDY AREA

Airborne radar surveys were done in Ragnhild Glacier basin (RGB) and Shirase Glacier basin (SGB) as sketched in Figure 1. We assume that the ice flows in the direction of surface slope, which is consistent with ground surveys at many sites in these regions (Takahashi and others, 1997). Because the radar polarization plane is always along the flight path (see section 3), the angle θ between the flow and the flight path equals the angle between the flow and the polarization plane.

Table 1. Locations of the flight turning points

Site	*Location*
R1	71.7° S, 35.9° E
R2	72.6° S, 31.4° E
R3	73.3° S, 31.7° E
S1	70.2° S, 38.4° E
S2	71.0° S, 39.8° E
S3	71.0° S, 41.1° E
S4	70.6° S, 41.1° E

Our 480 km long survey path in RGB is triangular. The line starts at the Yamato Mountains (site R1), which is near the ice divide between RGB and SGB, and crosses the main ice flow in RGB on the way to the Belgica Mountains (site R2). This segment is 184 km long and roughly perpendicular to the ice flow ($\theta = 70$–$80°$). Following this segment, the airplane headed inland. The second segment, from R2 to R3, is 73 km long and θ is roughly 0°. The third segment, from R3 to R1, is 222 km long and θ increases from 30° to 60° towards R1. The other study line, in SGB, is 195 km long. The first segment, between sites S1 and S2, is from Shirase Glacier to the inland region. The angle θ is 45° near site S1, but decreases rapidly to 10–20° along the route to S2 and reaches 0° near site S2. Between S2 and S3, $\theta > 70°$. Between S3 and S4, θ is 40–50°.

These two study lines cover three distinct ice-flow features. The first one is parallel flow. Regional-scale ($\sim 10^2$ km) surface topography suggests that the ice flows parallel from the inland divide to the central part of segments R1–R2 and R3–R1. As segments R1–R2 and R3–R1 inclined 70–80° and 30–60° to the flow, respectively, we observed the parallel-flow region with this range of θ.

The second flow type is longitudinal compression on the stoss side of nunataks. In general, nunataks and the accompanying shallow bedrock form a barrier to ice flow and cause an ice ridge on the stoss side. Such an ice ridge can be recognized at the Belgica Mountains where there are three major nunataks in a 10×20 km^2 area. A bare-ice field with a meteorite trap, which is evidence for emergent ice, was found only on the lee side (Kojima and others, 1981). Thus, we assume that vertical strains are small compared with longitudinal compression and transverse extension at the ice ridge on the stoss side. This area includes the segment R2–R3 and some portions of R3–R1. The polarization plane for the segment R2–R3 is longitudinal.

The third flow type is convergent flow towards an ice stream (Naruse, 1978). We travelled through this area in SGB with a longitudinal polarization for the segment S1–S2 and transverse polarization for the segment S2–S3–S4. This region has more convergent flow than in our previous, higher-elevation, ground-based survey in this drainage basin (Fig. 1).

3. RADAR METHOD

The radar survey was done in 1986 with a pulse-modulated airborne system. A linearly polarized transmitting antenna

was suspended under one wing, and a linear-polarized receiving antenna was under the other wing. The polarization plane here is always parallel to the flight-line. Other specifications of this radar system are listed in Table 2. Only 179 MHz radar data are available along these study lines.

The radar echoes were recorded as a time series of the received power P_r. In general, P_r is affected by dielectric properties of ice and radar system parameters. For a given depth z and polarization plane θ, the radar equation gives

$$P_r = \frac{S}{(h + z/\sqrt{\varepsilon})^2} \frac{B\sigma}{L}. \quad (1)$$

This equation is modified from that in Matsuoka and others (2003) to account for the airplane height above the ground h, which ranged between 150 and 300 m. S represents various system parameters that consist of transmitting power, antenna gain, antenna beamwidth, and wavelength. The ice properties include permittivity of ice $\varepsilon = 3.15$, loss factor L, back-scattering cross-section σ and birefringence.

If the c axes are not parallel to the wave-propagation axis, then the ice sheet is birefringent and an incident radio wave separates into two components within the ice. When the waves reach the ice-sheet surface after being scattered, they superimpose either constructively or destructively, depending on their phase difference. In Equation (1), B is a measure of birefringence, a power level relative to the maximum P_r, which is observed when the two components are in phase; B in decibels is always negative. Since L is independent of θ, the dependence of P_r on θ can come only from B, σ and ε. However, anisotropy from ε in the term $(h + z/\sqrt{\varepsilon})^2$ is less than ~0.1 dB and thus will be ignored.

Table 2. Specifications of the 179 MHz radar system. See Uratsuka and others (1996) for more details

Transmitter	Transmitting power	+60 dBm
	Pulse width[a]	60/250/1000 ns
Receiver	Detection limit[a]	−98/−103/−108 dBm
Antenna	Type	Three-element Yagi
	Beam width	70° in E-plane[b]
		90° in H-plane[b]
Wavelength in ice		0.94 m
Vertical resolution in ice[a,c]		5/21/84 m

[a] Detection limit and vertical resolution depend on the pulse width.

[b] E-plane is in the flight direction, and H-plane is perpendicular to the flight direction.

[c] Vertical resolutions are the wave travel distances for half of the pulse widths.

Small instabilities in the transmitting power and the receiving-amplifier gain result in statistical errors in P_r of <1 dB. To determine the bedrock topography, we used 60, 250 and 1000 ns pulse widths in RGB. In contrast, only the 250 ns pulse width was used in SGB. We compensated for variations in h and the changes of transmitting power that occurred when we changed the pulse width. Also, we used the propagation speed of 169 m μs^{-1} to convert the two-way travel time to the depth.

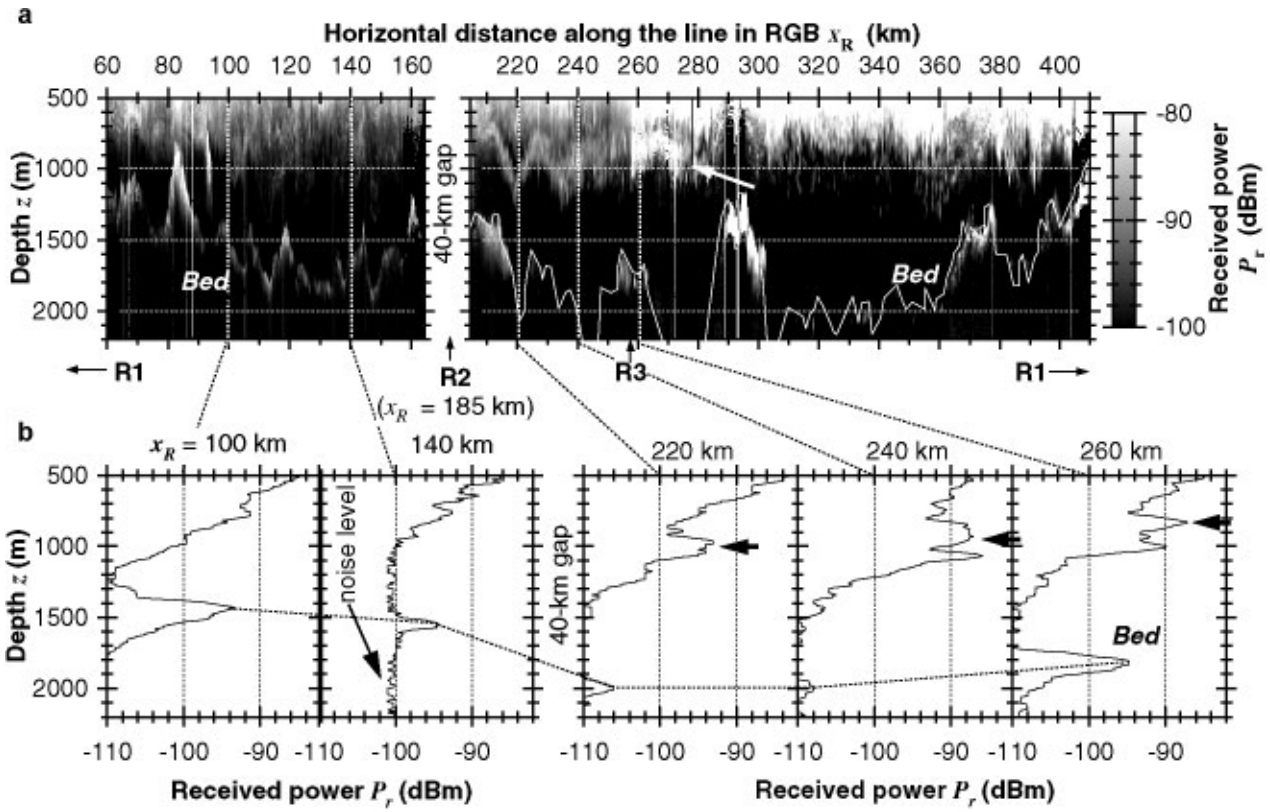

Fig. 2. Radar echo along the survey line in RGB. (a) Radargram. Locations of R1–R3 correspond to the sites shown in Figure 1b. R1 is at $x_R = 0$ and 480 km. The gray scale on the right is for P_r. The continuous, jagged white line in the right panel highlights the bed topography where scattering from the bed is not obvious. A white arrow marks the high-P_r zone, a zone of relatively high internal P_r. (b) Depth profiles of P_r at $x_R = 100$, 140, 220, 240 and 260 km from left to right. The dotted line connects the bed depth at the different positions. Black horizontal arrows at $x_R = 220$, 240 and 260 mark the high-P_r zone. Detection limit ranges from −98 to −108 dBm, depending on the pulse width (Table 2).

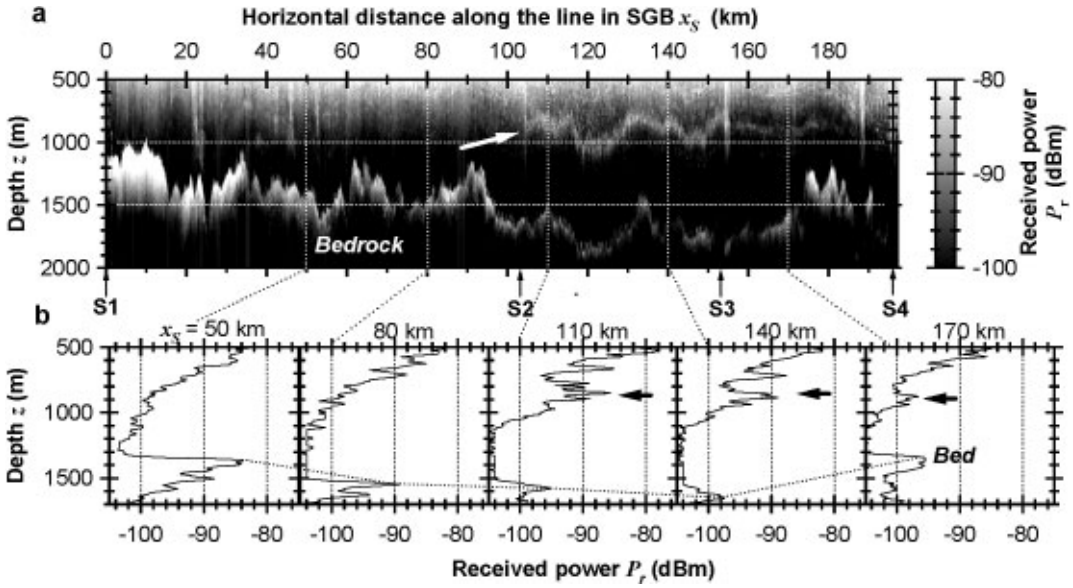

Fig. 3. Radar echo along the survey line in SGB. (a) Radargram. Locations of S1–S4 correspond to the sites shown in Figure 1b. The white arrow marks the distinct high-P_r zone. The gray scale on the right represents P_r. (b) Depth profiles of P_r at x_S = 50, 80, 110, 140 and 170 km from left to right. The dotted line connects the bed depth at the different positions. Black horizontal arrows at x_S = 110, 140 and 170 km mark the high-P_r zone. Detection limit is at −103 dBm (Table 2).

Ice-sheet surface undulations from sastrugi and crevasses can cause off-nadir reflections that get mixed up with the internal scattering that we seek. To estimate a maximum depth below which this is not a problem, we assume $h = 300$ m and a 1000 ns pulse width. In this case, we estimate that off-nadir surface reflections with an incident angle of 77° have the same two-way travel time as the nadir reflections from 500 m depth. Therefore, as the antenna beamwidth is 70–90° (Table 2), all features in the radar echoes below 500 m, on which we will focus in this paper, should not be from surface undulations. Therefore, surface undulations are not a problem in this study.

4. RESULTS

In the vicinity of sites R1 and R2, the ice thickness abruptly changes from about 1000 m to about 500 m and decreases quickly near some nunataks. That causes some echoes from the off-nadir bed that mix with the internal scattering. Thus, we discuss only the radar echoes 60–70 km or more from R1 and 20 km or more from R2. There were no such restrictions in SGB.

4.1. Parallel-flow region

Radar echoes along the line in RGB are shown in Figure 2. Ice flows parallel to the Princess Ragnhild Coast ice shelf in the central part of paths R1–R2 and R3–R1. For $60 < x_R < 165$ km and $280 < x_R < 410$ km, P_r gradually decreases with increasing depth. Vertical profiles of P_r (Fig. 2b) show small P_r peaks (e.g. $z = 800$ m, $x_R = 100$ km), but these peaks are isolated in horizontal extent and thus do not constitute extensive layers that can readily be analyzed. The polarization plane is nearly perpendicular to the ice flow with $\theta = 70$–80° in R1–R2 and $\theta = 30$–60° in R3–R1. Despite this range of θ, no distinct layers were found in these parallel-flow regions.

4.2. Longitudinal compression on the stoss side of nunataks

In contrast to the parallel-flow region, a distinct zone of relatively high P_r emerges at depths of 700–1200 m on the stoss side of the nunataks from R2 to R3 (Fig. 2a). The thickness of the high-P_r zone decreases from 200–400 m to less than about 200 m as the ice approaches the nunataks around R2. In addition, it maintains a nearly constant distance over the underlying bed. The radar polarization is longitudinal between R2 and R3. A high-P_r zone also exists about 10–20 km from R3 towards R1. Further from R3, P_r becomes less distinct and disappears.

Vertical P_r variations (Fig. 2b) show that the high-P_r zone has an amplitude of about 6 dB over that of the ice immediately above it and that the peak values are about 15–20 dB above the detection limit of −108 dBm (Table 2). Figure 2a shows that these numbers are typical for $205 < x_R < 270$ km. The depth profiles at x_R = 220, 240 and 260 km in Figure 2b show that the high-P_r zone has several P_r peaks. However, the depths of P_r peaks at these three sites do not correlate with each other, and no individual continuous layers were apparent within the high-P_r zone in the radargram.

4.3. Convergent-flow region toward an ice stream

Radar echoes along the line in SGB are shown in Figure 3. P_r along the segment S1–S2 gradually decreases with increasing depth. However, starting near site S2, where the flight path abruptly changed by about 90° such that the polarization became roughly perpendicular to the flow with $\theta > 70°$, a distinct zone of relatively high P_r appears. This zone is at 800–1100 m depth. It continues to site S3. After site S3, where the flight path changed again, this high-P_r zone weakens and vanishes before site S4. Thus, this distinct high-P_r zone is continuous for >80 km and maintains a nearly constant distance above the underlying bed, even as the bed changes elevation by 300 m. The only difference in

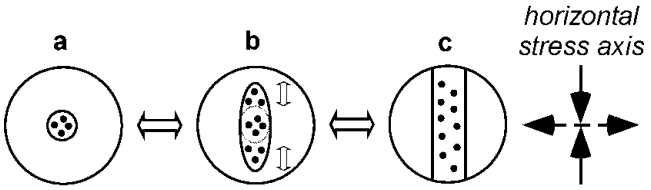

Fig. 4. COF patterns inferred from the observed radar echoes. All diagrams are projected onto the horizontal plane. (a) Strong vertical single pole. (b) Elongated single pole. (c) Vertical girdle. For (b) and (c), the cluster plane of c axes is along the compression axis and perpendicular to the extension axis. Large scattering occurs only along the horizontal compression axis when COF patterns alter among (a–c), or if elongations of (b) change.

observation parameters between segments S1–S2 and S2–S3–S4 is the polarization plane orientation relative to the ice-flow direction.

Vertical profiles of P_r at five sites are shown in Figure 3b. At $x_S = 110$ km (near site S2) and 140 km (near site S3), the high-P_r zone is 200–300 m thick and is stronger than the signal from the ice above by 8 dB. Figure 3a shows that this thickness and contrast in P_r is typical between sites S2 and S3. At $x_S = 1170$ km, which is between S3 and S4, the high-P_r zone is thinner and weaker than between S2 and S3. The P_r contrast between the high-P_r zone and the ice above is several decibels.

4.4. Characteristics of the high-P_2 zone

The high-P_r zones emerge both in the stoss side of the nunataks and in the convergent-flow region for >60 km (Fig. 1b). They have some similar features. The zone is several hundred meters thick and keeps a nearly constant distance from the bed. In addition to these geometric features, the P_r contrast between the high-P_r zone and ice above is typically 6–8 dB, and P_r decreases monotonically below the high-P_r zone. The high-P_r zone on the stoss side was observed only with longitudinal polarization, whereas that in the convergent flow was observed with transverse polarization. In the next section, we argue that variable COF causes this polarization-dependent feature in regions where horizontal compression occurs.

5. DISCUSSION

We observed the high-P_r zone on the stoss side of the nunataks and in the convergent ice flow. We argue below that the high-P_r zone in both regions is caused by a similar mechanism.

5.1. Causes of the high-P_2 zone and its polarization dependence

The major causes of radio-wave scattering within ice are acidity, density and COF non-uniformities. Large acidity non-uniformities, which are usually due to volcanic eruptions (Hammer, 1980), cause radio-wave scattering from high-acid layers throughout the entire ice sheet except for some portions near the bed (Miller, 1981). Density non-uniformities are smoothed out with increasing depth, and air bubbles turn into air hydrates. For the estimated temperature around S2 (Nishio and others, 1989), this transformation should occur at about 600 m (Miller, 1969). The permittivity of N_2 hydrate, at about 2.8 (Gough, 1972), is significantly smaller than that of ice; however, because of its negligible volume fraction in ice ($<10^{-3}$), air-hydrate non-uniformities cannot cause any permittivity changes significant for radio-wave scattering. Although density non-uniformities are insignificant below a certain depth, COF non-uniformities are stronger at greater depths. In addition to the gradual development of COF clustering with depth, abrupt changes of COF exist in ice cores including Dome Fuji at the head of RGB and SGB (see brief review in Fujita and others, 2003).

We focus here on the distinct zone of relatively high P_r only at depths exceeding 700 m. At 179 MHz, the Fresnel reflectivities derived from dielectric measurements of ice suggest that radio-wave scattering is largely caused by permittivity non-uniformities due to density and COF variations (Fujita and Mae, 1994). A simple calculation on the Fresnel reflectivities (Paren, 1981) shows that the observed P_r contrast of about 6 dB between the high-P_r zone and adjacent ice above (Figs 2 and 3) can be explained only when density variations exceed 7 kg m^{-3}. This is equivalent to −64 dB when the ordinary reflectivities are about −70 dB. This 7 kg m^{-3} is much larger than the maximum density fluctuation of 1 kg m^{-3} at 1000 m in the Byrd core (Clough, 1977), which will be about 1.4 kg m^{-3} at 700 m depth under the glaciostatic pressure assuming that the air included in the ice follows the ideal gas equation. Therefore, it is unlikely that density non-uniformities cause the observed P_r contrast. On the other hand, COF non-uniformities seem to dominate the scattering signal at depths exceeding about 400 m for a radar frequency of 179 MHz in SGB (Fujita and others, 2003; Matsuoka and others, 2003). Furthermore, we estimate below that possible COF alternations give P_r contrast in good agreement with the measurements. Thus, we argue that the most likely cause of the high-P_r zone both on the stoss side of nunataks and in the convergent-flow region is permittivity non-uniformities due to COF variations.

The high-P_r zone emerges near site S2, where the flight path abruptly changed by about 90°. Although we did not examine the ice at exactly the same location with two polarizations, the rotation of the airplane was completed within several seconds during which the airplane moved no more than several hundred meters. Hence, different polarizations were used at neighboring locations with similar flow. Furthermore, the height of the airplane was steady at about 300 m near S2. This dependence on polarization angle indicates that the high reflectivity in the high-P_r zone is due to a polarization anisotropy. Other explanations do not fit with the data. In particular, measurements of the balance velocity around site S2 indicate that S2 is outside of a distinct tributary of Shirase Glacier (Pattyn and Naruse, 2003); the balance velocity of 35 m a^{-1} at S2 is lower than those at other sites with a similar distance from the Shirase Glacier outlet. Also, we did not detect any abrupt changes in ice and bed topography near site S2 (Figs 1 and 3). Therefore, polarization anisotropy likely caused the high reflectivity.

Polarization anisotropy can be due to birefringence, backscattering or both (Equation (1)). We observed an 8 dB difference in P_r at two polarization planes roughly perpendicular to each other near site S2 (Fig. 3). Although these do not rule out birefringence, birefringence seems unlikely for the following reasons. If birefringence were the primary cause of anisotropy in P_r, then P_r would change sinusoidally with the polarization plane orientation and have a

maximum every 90° (Hargreaves, 1977). If the principal axes of birefringence were parallel or perpendicular to the flow direction, which is generally the case, then the birefringence would show equal intensities at the two polarizations because they are 90° apart. This would contradict our measurements. Furthermore, a previous radar survey with eight polarization planes in SGB (Fig. 1) showed that a high-P_r zone on two transverse profiles has its maximum only at one polarization plane orientation, showing that it is caused by anisotropic scattering due to certain one-axis-symmetric COF non-uniformities (Matsuoka and others, 2003).

Therefore, we conclude that the high-P_r zone in the convergent-flow region towards Shirase Glacier is caused by anisotropic COF scattering.

5.2. COF patterns in the high-P_r zone

Ice deformation occurs by dislocation glide accompanied by crystal rotation (Shoji and Higashi, 1978) under typical stresses and temperatures at middle depths of ice sheets. Because the *c* axes rotate away from the extension axis and cluster along the compression axis, various COF patterns can occur in ice sheets depending on strain configurations. Vertical single-pole patterns (Fig. 4a) generally occur under uniaxial compression and simple shear, whereas vertical-girdle patterns (Fig. 4c) generally occur under uniaxial extension (Azuma, 1994). Between these two extremes is the more common elongated single pole (Fig. 4b). Other complex COF patterns with multiple maxima are not considered, because they are mainly found near the base of ice sheets or in ice shelves (e.g. Budd and Jacka, 1989, fig. 3).

With these constraints, Matsuoka and others (2003) proposed from a multi-polarization radar survey along ice flow from Dome Fuji (Fig. 1a) that COF-pattern alternations between single pole and vertical girdle likely occur when horizontal compression occurs on single-pole fabric ice with various clustering. Single-pole fabric ice with weak clustering has a large number of crystal grains that have easy-glide planes close to the maximum shear stress direction. In contrast, the single-pole fabric ice with stronger clustering has a larger viscosity under the same stress and is stiffer. Thus, stronger single-pole fabric remains single-pole, but weaker single-pole fabric changes into vertical-girdle fabric. Prior clustering variations of single-pole fabric are found at Dome Fuji, the head of RGB and SGB (Azuma and others, 1999).

Spatial variations of the high-scattering zone (Fig. 1b) are consistent with theory and the above scenario. The ice ridge on the stoss side of the nunataks indicates local longitudinal compression and transverse extension. Thus, the *c* axes of deformed ice cluster in the longitudinal plane. In the convergent-flow region, the cluster plane will be transverse. Thus, it is most likely that COF alternations shown in Figure 4 occur where we found the anisotropic, high-P_r zone. The alternations give larger and smaller P_r, when the polarization plane is parallel and perpendicular to the compression axis, respectively. This is consistent with the observed anisotropy. Furthermore, the observed large anisotropy of about 8 dB near site S2 can occur provided we assume that COF patterns alter between single pole and vertical girdle (Matsuoka and others, 2003). Thus, we interpret the high-P_r zone as being caused by COF alternations as sketched in Figure 4, which will be construed as ice-flow features and their history in section 5.3.

5.3. Spatial variation of the high-P_r zone

In addition to the distinct high-P_r zone along the ice ridge, the less distinct high-P_r zone was found for 10–20 km in the northeastern slope from the ridge. This suggests that the Belgica Mountains, which consist of three major nunataks in a $10 \times 20\ km^2$ area, and the accompanying shallow bedrock cause anisotropic ice structures over an area on the stoss side at least 85 km long and 20 km wide.

A distinct high-P_r zone is lacking for various polarizations along paths R1–R2 and R3–R1, where ice flows parallel. Thus, COF alternations such as those sketched in Figure 4 do not exist in the parallel-flow region. Although elongated single-pole fabrics tend to form under pure shear (e.g. Azuma, 1994), COF alternations in this region are not developed enough to cause distinct internal scattering zones. Geological evidence from the Sør Rondane Mountains (Fig. 1a) where ice flow is parallel shows insignificant variation of ice-sheet elevation for the last 10^6 years (Moriwaki and others, 1992). This suggests that the parallel-flow areas that cross paths R1–R2 and R3–R1 have similar stress configurations induced by the current ice topography. Thus, we attribute this lack of a high-P_r zone to the past and present ice flow.

The high-P_r zone was observed in the convergent-flow region for 80 km, roughly along 1800 m a.s.l. in this study, and for over 300 km along 2200 m a.s.l. and 20 km along 2600 m a.s.l. for the previous study marked in Figure 1. Thus, we argue that the high-P_r zone spreads over a large area in the lower reaches of the convergent-flow region. If we assume that the age of the high-P_r zone along S2–S3 is the same as that of the high-P_r ice at roughly the same depth in the previous study (about 12 000 years) and if we apply current surface ice-flow speed variations along 40° E (Nishio and others, 1989), then the high-P_r ice along the segment S2–S3 was originally deposited about 210 km upstream in the upper part of the current convergent-flow region. However, the stacking of ice with single pole and vertical girdle requires a prior clustering variation in single-pole, which is unlikely to occur in the convergent-flow sector. Thus, the high-P_r zone found along 1800 m a.s.l. in this study can be explained by the same mechanism as that for the 2200 and 2600 m a.s.l. ice in the previous study only if the ice 210 km upstream from S2–S3 had been out of the convergent-flow sector in the past. This condition is needed so that single-pole fabrics with clustering variations could have formed, which then would turn into alterations of single-pole to vertical-girdle COF. This agrees with the ice-core studies at Mizuho (X in Fig. 1a) that indicate that the lower part of SGB has thinned by up to 350 m since 2000 years ago, and the upper boundary of the convergent-flow region was at a lower elevation in the past (Kameda and others, 1990).

According to the data in Figure 3, the P_r peak amplitude at $x_s = 170$ km (along S3–S4) is a quarter of that at $x_s = 110$ and 140 km (along S2–S3). If we assume that reflectivities depend on θ sinusoidally due to COF alternations between single pole and vertical girdle, the predicted ratio of the amplitude along segments S2–S3 and S3–S4 is 9:7, which is much less than the observed 4:1 ratio. Moreover, the relatively weak high-P_r zone disappears entirely at $x_s = 180$ km, even though the polarization was kept the same along the path. A similar absence of radar-reflecting layers occurs in some tributaries of Bindschadler Ice Stream (former Ice Stream D), West Antarctica (Siegert and others, 2003). Bed topography is unlikely to cause this

disappearance, because spatial variations of the high-P_r zone do not correlate significantly with bed topography for over 300 km (Matsuoka and others, 2003). In addition to regional-scale ice topography, changes in the bed conditions may cause changes in the flow that produce COF-based echoes. At a transition between basal sliding and non-sliding, the stress configuration changes within ice (Weertman, 1976). The ice-sheet topography between line A and segment S3–S4 has features that indicate that the ice between S3 and S4 flows from a part of the less distinct high-P_r zone along line A (Fig. 1b). Thus, we suggest that a tributary of fast-flowing ice with faster basal flow may penetrate inland across segment S3–S4 from the fast-flowing Shirase Glacier. Balance-velocity estimates indicate that a tributary of Shirase Glacier is near S3 and the tributary becomes indistinct at about 1700 m a.s.l. (Pattyn and Naruse, 2003). Modelling efforts to characterize regional-scale COF developments in conjunction with precise mapping of tributaries by satellite ice-flow measurements will give insights into how stream-flows become onset.

6. CONCLUSIONS

In our radar survey in eastern Dronning Maud Land, we found that when the polarization was across the ice flow, a distinct zone of relatively large radar echoes at depths of 700–1200 m occurred in convergent flow but not in parallel flow. A similarly distinct zone was found on an ice ridge impeded by nunataks. Thus, we detected large radar echoes in these two areas only when the polarization plane was parallel to the compression axis of ice. We concluded that this zone is caused not by birefringence but by anisotropic scattering. The most likely cause of this anisotropic scattering is COF alternations. If COF patterns alternate between single-pole and vertical-girdle, or, more generally, two elongated single poles with different elongations, then a large reflectivity would occur only along the polarization plane parallel to the compression axis as observed. Thus, we argue that the primary cause of the observed patterns is past and present flow features induced by ice topography (i.e. longitudinal compression with nunataks, convergent flow and parallel flow) and basal conditions.

In this study, we found that the orientation of the polarization plane relative to the principal stress can reveal information about the ice structure within wide areas of ice sheets. In particular, our high-frequency radar detected spatial variation of distinct COF patterns that are related to the deformational history of ice, information on which can be used to predict the deformation rate in the future. Therefore, airborne radar at high frequencies has a high potential to map anisotropic ice structures over wide areas, which can complement evidence from ice cores and geological studies to gain a better understanding of the dynamic behavior of ice sheets.

ACKNOWLEDGEMENTS

Radar data were obtained by the 27th Japanese Antarctic Research Expedition; we thank all of the participants. We are indebted to C. F. Raymond for helpful comments on a first draft of this paper, C. Bentley and an anonymous referee for critical remarks during reviewing, and J. Glen for his efforts as scientific editor. K.M. was supported by a research fellowship from the Japan Society for the Promotion of Science.

REFERENCES

Azuma, N. 1994. A flow law for anisotropic ice and its application to ice sheets. *Earth Planet. Sci. Lett.*, **128**(3–4), 601–614.

Azuma, N. *and 6 others*. 1999. Textures and fabrics in the Dome F (Antarctica) ice core. *Ann. Glaciol.*, **29**, 163–168.

Budd, W. F. and T. H. Jacka. 1989. A review of ice rheology for ice sheet modelling. *Cold Reg. Sci. Technol.*, **16**(2), 107–144.

Clough, J. W. 1977. Radio-echo sounding: reflections from internal layers in ice sheets. *J. Glaciol.*, **18**(78), 3–14.

Fujita, S. and S. Mae. 1994. Causes and nature of ice-sheet radio-echo internal reflections estimated from the dielectric properties of ice. *Ann. Glaciol.*, **20**, 80–86.

Fujita, S., S. Mae and T. Matsuoka. 1993. Dielectric anisotropy in ice Ih at 9.7 GHz. *Ann. Glaciol.*, **17**, 276–280.

Fujita, S. *and 6 others*. 1999. Nature of radio-echo layering in the Antarctic ice sheet detected by a two-frequency experiment. *J. Geophys. Res.*, **104**(B6), 13,013–13,024.

Fujita, S., K. Matsuoka, H. Maeno and T. Furukawa. 2003. Scattering of VHF radio waves from within an ice sheet containing the vertical girdle type ice fabric and anisotropic reflection boundaries. *Ann. Glaciol.*, **37**, 305–316.

Gough, S. R. 1972. A low temperature dielectric cell and the permittivity of hexagonal ice to 2 K. *Can. J. Chem.*, **50**(18), 3046–3051.

Hammer, C. U. 1980. Acidity of polar ice cores in relation to absolute dating, past volcanism, and radio-echoes. *J. Glaciol.*, **25**(93), 359–372.

Hargreaves, N. D. 1977. The polarization of radio signals in the radio echo sounding of ice sheets. *J. Phys. D*, **10**(9), 1285–1304.

Kameda, T., M. Nakawo, S. Mae, O. Watanabe and R. Naruse. 1990. Thinning of the ice sheet estimated from total gas content of ice cores in Mizuho Plateau, East Antarctica. *Ann. Glaciol.*, **14**, 131–135.

Kojima, H., K. Yanai and T. Nishida. 1981. *Belgica Mountains. 1:25 000.* Tokyo, National Institute of Polar Research.

Liu, H., K. C. Jezek and B. Li. 1999. Development of an Antarctic digital elevation model by integrating cartographic and remotely sensed data: a geographic information system based approach. *J. Geophys. Res.*, **104**(B10), 23,199–23,213.

Matsuoka, K. *and 6 others*. 2003. Crystal-orientation fabrics within the Antarctic ice sheet revealed by a multi-polarization-plane and dual frequency radar survey. *J. Geophys. Res.*, **108**(B10), 2499. (10.1029/2002JB002425.)

Miller, D. H. M. 1981. Radio-echo layering in polar ice sheets and past volcanic activity. *Nature*, **292**(5822), 441–443.

Miller, S. L. 1969. Clathrate hydrates of air in Antarctic ice. *Science*, **165**(3892), 489–490.

Moriwaki, K., K. Hirakawa, M. Hayashi and S. Iwata. 1992. Late Cenozoic history in the Sør Rondane Mountains, East Antarctica. *In* Yoshida, Y., K. Kaminuma and K. Shiraishi, *eds. Recent progress in Antarctic earth science.* Tokyo, Terra Scientific Publishing Co., 661–667.

Naruse, R. 1978. Surface ice flow and strain of the ice sheet measured by a triangulation chain in Mizuho Plateau. *Nat. Inst. Polar Res. Mem., Ser. Special Issue*, **7**, 198–226. [In English with Japanese summary.]

Nishio, F., S. Mae, H. Ohmae, S. Takahashi, M. Nakawo and K. Kawada. 1989. Dynamical behaviour of the ice sheet in Mizuho Plateau, East Antarctica. *Proc. NIPR Symp. Polar Meteorol. Glaciol.*, **2**, 97–104.

Paren, J. G. 1981. Correspondence. Reflection coefficient at a dielectric interface. *J. Glaciol.*, **27**(95), 203–204.

Pattyn, F. and R. Naruse. 2003. The nature of complex ice flow in Shirase Glacier catchment, East Antarctica. *J. Glaciol.*, **49**(166), 429–436.

Shoji, H. and A. Higashi. 1978. A deformation mechanism map of ice. *J. Glaciol.*, **21**(85), 419–427.

Siegert, M. J. and S. Fujita. 2001. Internal ice-sheet radar layer profiles and their relation to reflection mechanisms between Dome C and the Transantarctic Mountains. *J. Glaciol.*, **47**(157), 205–212.

Siegert, M. J. and R. Kwok. 2000. Ice-sheet radar layering and the development of preferred crystal orientation fabrics between Lake Vostok and Ridge B, central East Antarctica. *Earth Planet. Sci. Lett.*, **179**(2), 227–235.

Siegert, M. J., A. J. Payne and I. Joughin. 2003. Spatial stability of Ice Stream D and its tributaries, West Antarctica, revealed by radio-echo sounding and interferometry, *Ann. Glaciol.*, **37**, 377–382..

Takahashi, S. *and 6 others*. 1997. Ice sheet dynamics. *In Antarctica: East Queen Maud Land/Enderby Land glaciological folio.* Tokyo, National Institute of Polar Research, Sheet 6.

Uratsuka, S., F. Nishio and S. Mae. 1996. Internal and basal ice changes near grounding line derived from radio-echo sounding. *J. Glaciol.*, **42**(140), 103–109.

Weertman, J. 1976. Sliding–no-sliding zone effect and age determination of ice cores. *Quat. Res.*, **6**(2), 203–207.

MS received 23 July 2003 and accepted in revised form 13 February 2004